

## ORIGINAL RESEARCH ARTICLE

# Simultaneous multichannel multi-offset ground-penetrating radar measurements for soil characterization

Manuela Sarah Kaufmann  | Anja Klotzsche  | Harry Vereecken  | Jan van der Kruk

Agrosphere (IBG-3), Institute of Bio- and Geosciences, Forschungszentrum Jülich, Jülich, 52428, Germany

## Correspondence

M. S. Kaufmann, Agrosphere (IBG-3), Institute of Bio- and Geosciences, Forschungszentrum Jülich, 52428 Jülich, Germany.  
Email: kaufmannmanuela@hotmail.com

## Funding information

Bundesministerium für Bildung und Forschung, Grant/Award Number: 031B0026C

## Abstract

For vadose zone studies, it is essential to characterize the soil heterogeneity. However, manual soil coring is time consuming and lacks spatial coverage. Ground-penetrating radar (GPR) has a high potential to map these parameters. However, with conventional common-offset profile (COP) measurements, soil layer changes are only detected as a function of time, and no exact determination of velocities, and thus permittivity, is possible. For velocity estimation, time-consuming point-scale common midpoint (CMP) or wide-angle reflection and refraction (WARR) measurements are necessary. Recently, a novel simultaneous multi-offset multichannel (SiMoc) GPR system was released, enabling rapid profiling with virtually continuous acquisition of WARR gathers. For this system, we developed a new processing approach. First, time shifts caused by the different cables and receivers were eliminated by a novel calibration method. In the obtained CMP gathers, groundwave and (when present) reflection velocities were determined with an automated semblance approach. The obtained velocity can be converted to permittivity and soil water content. We tested SiMoc GPR with a synthetic study and time-lapse field measurements. In the synthetic study, the accuracy of velocity and layer thickness were within  $0.02 \text{ m ns}^{-1}$  and 2 cm. The SiMoc field results (spatial sampling of 5 cm) are consistent with coarse sampled single-channel data (spatial sampling of 10 m). Soil water content changes over the different measurement days were in agreement with nearby installed sensors (one per hectare). Overall, SiMoc GPR is a powerful tool for fast imaging of spatially highly resolved permittivity, and soil water content at a large scale.

## 1 | INTRODUCTION

Growing population and climate change are key challenges for the current and next generations, and it is therefore highly relevant to develop and establish innovative and sustainable management strategies to increase yields of agricultural products. One option is to divide agricultural fields into small-scale zones with similar soil properties and apply to each management zone optimized soil management (e.g., tillage),

**Abbreviations:** 2D, two-dimensional; 3D, three-dimensional; CMP, common midpoint; COP, common-offset profile; EMI, electromagnetic induction; ERT, electrical resistivity tomography; GPR, ground-penetrating radar; HMO, hyperbolic move-out; LMO, linear move-out; Rx, receiver; SiMoc, simultaneous multi-offset multichannel; SWC, soil water content; TDR, time-domain reflectometry; TERENO, Terrestrial Environmental Observatories; Tx, transmitter; WARR, wide-angle reflection and refraction.

This is an open access article under the terms of the Creative Commons Attribution License, which permits use, distribution and reproduction in any medium, provided the original work is properly cited.

© 2020 The Authors. *Vadose Zone Journal* published by Wiley Periodicals, Inc. on behalf of Soil Science Society of America

fertilization, and/or irrigation to increase production (Cherici, Kuang, Poletti, & Rucci, 2012). For defining these different zones, highly resolved soil property or state maps of features like soil texture, soil water content (SWC), and soil salinity are necessary (Srinivasan, 2006). Conventional mapping techniques like soil coring or soil pits are invasive, expensive, time consuming, and lack lateral resolution. Remote sensing methods can be used as input. However, their sensitivity is mainly limited to the upper few centimeters (Vereecken et al., 2008).

In contrast, geophysical methods allow rapid and noninvasive mapping of soil characteristics that can be used as proxy data for any soil properties of interest (Dabas & Tabbagh, 2003). Mainly, electromagnetic methods like electromagnetic induction (EMI; Corwin & Lesch, 2005), electrical resistivity tomography (ERT; Brunet, Clement, & Bouvier, 2010), and ground-penetrating radar (GPR; Huisman, Hubbard, Redman, & Annan, 2003; Klotzsche, Jonard, Looms, van der Kruk, & Huisman, 2018) are used to characterize the upper few meters of agricultural soils. The obtained (apparent) electrical conductivity ( $\sigma$ ) or resistivity ( $\rho$ ,  $\sigma = 1/\rho$ ) measured by EMI and ERT, respectively, depend on many soil parameters like SWC, clay content, and salinity (Corwin & Lesch, 2005). To disentangle the different influences, ground truth soil samples, other measurement methods (e.g., gamma-ray), or time-lapse measurements are needed (Adamchuk, Hummel, Morgan, & Upadhyaya, 2004).

In comparison, GPR has the advantage to map stratigraphic layers with physical contrast in dielectric permittivity ( $\epsilon_r$ ) and electrical conductivity ( $\sigma$ ) (Weihermüller, Huisman, Lambot, Herbst, & Vereecken, 2007). The dielectric permittivity is correlated to the velocity of the electromagnetic wave and can be linked to SWC with empirical equations (Topp, Davis, & Annan, 1980) or physical mixing models (Roth, Schulin, Fluhler, & Attinger, 1990). The electrical conductivity is linked to the attenuation and amplitude of the electromagnetic waves and can be correlated to soil texture and clay content (Busch, Van der Kruk, & Vereecken, 2014). Additionally, due to the use of higher frequencies compared to ERT and EMI, a higher image resolution can be obtained. However, in areas with highly conductive soils (e.g., clay), the GPR signal is strongly attenuated and limits penetration depths and thus the use of GPR (Huisman, Sperl, Bouten, & Verstraten, 2001). In these areas, EMI can be used complementarily to GPR for soil characterization (De Benedetto et al., 2012).

Traditionally, surface GPR measurements are performed with single-channel instruments, using one transmitter (Tx) and one receiver (Rx) antenna. A standard measurement method is to place the Tx and Rx with a fixed offset in a sledge, and by pulling or pushing the sledge, so-called common-offset profiles (COP) are collected. The COPs are used to detect anthropogenic elements like pipes (Pettinelli et al., 2009), layer thickness or changes in soils, ice, or sediments (Brandt, Langley, Kohler, & Hamran, 2007), and bedrock depths

### Core Ideas

- A novel approach to obtain high spatial resolution of soil properties is shown.
- The soil was characterized along a transect with changing soil texture.
- An automatized semblance picking of ground wave velocity to determine soil water content is shown.
- Time-lapse measurements reveal soil water content changes along a profile.

(Neal & Roberts, 2000). However, the recorded signals are measured in time, and observed differences in travel time can be related to changes in permittivity and/or layer thickness variations. For an exact depth and permittivity estimation, subsurface velocity information is essential. The distribution of subsurface velocity changes can be obtained with multi-offset measurements like common midpoint (CMP), or wide-angle reflection and refraction (WARR) gathers at specific locations along the COP. Thereby, the Tx and Rx antennas are placed on the surface with changing offset. Common midpoint or WARR measurements are time consuming and are mostly performed at sparse locations. Additionally, many commercial GPR systems are monostatic (Tx and Rx in one box), and velocity information can only be obtained at locations with hyperbolas, caused by surface scatters with contrasting permittivity such as stones or holes (Jol, 2008). In both cases, the limited velocity information is assumed to be representative for larger areas. This results in low spatial resolution of subsurface velocity, resulting in possible errors in estimated layer thickness, soil permittivity, and hence SWC.

The permittivity of the soil can also be obtained by assuming or knowing the real depth of a reflector in a COP, or by analyzing the ground wave velocity (Huisman et al., 2003). The groundwave travels directly between the Tx and Rx antennas in the upper few centimeters of the subsurface. The sensing depth of the groundwave depends mainly on the dominant wavelength of the electromagnetic wave, in addition to the soil type and SWC. Therefore, in GPR systems with lower center frequency, the sampling depth is larger than in systems with higher frequencies (van Overmeeren, Sariowan, & Gehrels, 1997). However, with both methods (known depth and groundwave), only the permittivity or velocity of the topsoil can be obtained. Furthermore, for ground wave analysis, the COP data need to be acquired with an antenna offset large enough to avoid interference between direct ground wave and airwave and small enough to have a sufficiently strong amplitude. Determining the right antenna offset prior to measurements can be difficult, especially for field sites with

changing soil characteristics (Huisman et al., 2001; Oimbe, Ingle, & Awale, 2018). Therefore, permittivities obtained from single-channel GPR measurements are either lacking spatial or vertical resolution, are time consuming to measure (CMP or WARR), or require prior knowledge of the field site.

In the last decade, several multichannel GPR systems have been developed to overcome these issues. Commonly, these multichannel systems use multiple common-offset Tx and Rx pairs for faster and denser sampling (Trinks et al., 2018), often called three-dimensional (3D) GPR. Another option is to use multichannel GPR systems for multi-offset recordings, with one Tx and multiple Rx's with different offsets inline, similar to seismic systems. Such systems can measure WARR gathers with a high spatial resolution. Due to the possibility to extract detailed velocity information, seismic processing and imaging techniques can be applied to increase the signal-to-noise ratio and depth information of profiles (Forte & Pipan, 2016). Until now, these multichannel systems measured each Rx and offset separately (multiplexed) with a sampling delay, resulting in either a slow measurement speed or in WARR gathers without constant Tx position (Wollschläger, Gerhards, Yu, & Roth, 2010). Additionally, doubts about the limited offsets (traces) for velocity analysis hindered large-scale multi-offset studies (Trinks et al., 2018).

Several studies with either customary multichannel systems (Wollschläger et al., 2010) or combining time-consuming single-channel measurements (Berard & Maillol, 2007) exist. For example, as one of the first, Fisher, McMechan, and Annan (1992) collected common Rx gathers with 40 traces by manually moving the Tx at each location and processed the data with standard seismic software to obtain a migrated profile with high signal to noise ratio. With a similar approach, Bradford (2006) acquired two-dimensional (2D) multi-offset data and used reflection tomography on the normal move-out, stacked, post-migrated profile for enhanced interpretation and determination of SWC (Bradford, 2008). The same processing steps were used on data measured with a new multichannel adapter with four Rx's and repeating the measurements with different offsets to estimate soil porosity (Bradford, Clement, & Barrash, 2009) and glacier SWC (Bradford, Nichols, Mikesell, & Harper, 2017). However, as the adapter between the antennas did not allow simultaneous measurements, each offset was measured with a different Tx location, and hence the data were binned over 0.5 m. A sequentially measuring multichannel system with two monostatic antenna pairs was used by Gerhards et al. (2008). In the obtained COPs (three different offsets), reflectors were picked, and all obtained travel times were used in an inversion to obtain the relative dielectric permittivity of the soil and the depth and inclination angle of the reflector for every position along the profile. Wollschläger et al. (2010) extended this method by recording seven different offsets with three antenna pairs and concluded that with multi-offset

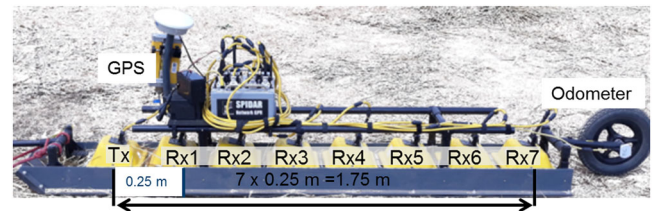


**FIGURE 1** Picture of the WARR-machine used for simultaneous multi-offset multichannel (SiMoc) ground-penetrating radar (GPR). The transmitter (Tx) and seven receivers (Rx's) are placed in a plastic sledge with an antenna separation of 0.25 m. The largest offset between Tx and Rx7 is 1.75 m. The odometer triggers all seven receivers simultaneously. All positions are recorded with high-precision GPS at the midpoint between Tx and Rx1

data, changes in travel time could be related to changing soil permittivity, rather than exclusively to depth changes of a reflector. The same system was used to obtain SWC distribution at field scale in the Gurbantuüngguüt Desert (Qin et al., 2013), and to map permafrost features (Pan et al., 2014). Even though all these results look promising, all approaches have some issues: combining single-channel measurements (Bradford, 2006; Fisher et al., 1992) is time consuming, using monostatic antennas (Gerhards et al., 2008) hinders flexible usage, and time delays between different offset measurements (Bradford et al., 2017) decrease the spatial resolution.

Recently, new technology developments allow measuring multiple channels simultaneously. Therefore, multichannel systems with multiple Rx's in a row can be used for direct WARR and CMP gathering (Trinks et al., 2018). For example, Muller (2018) used overlapping WARR gathers measured with noise-modulated 3D GPR equipment to predict depth, permittivity, and moisture content of road layers. However, his semiautomatic approach relies on continuous layers and is not suitable for soil characterization. A fully flexible multichannel system was developed by Sensors & Software (Mississauga, ON, Canada), allowing measuring with up to eight channels simultaneously (Annan & Jackson, 2017). The so-called “WARR-machine” uses one Tx and seven shielded 500-MHz PulseEKKO Rx's aligned (separation of 0.25 m) in a 2-m-long plastic sledge (Figure 1). Each measurement position is odometer triggered and recorded with a high-precision differential GPS (Trimble). This new system enables measurements of simultaneously multi-offset multichannel (SiMoc) GPR data at the same speed as one ordinary single-channel GPR COP. By simultaneously acquiring up to seven COPs (offsets 0.25–1.75 m), resulting in up to 10,000 WARR or CMPS gathers per hour, SiMoc GPR allows high-resolution mapping of changes in velocity, permittivity, and SWC at the field scale in a reasonable time (Diamanti, Elliott, Jackson, & Annan, 2018).

In this study, we deployed this fast measurement system at the field scale to investigate the potential and limitations

of SiMoc GPR data for soil characterization. Thereby, we investigate the necessary processing steps required to automatically analyze the large amount of measured data to provide highly spatially resolved changes in permittivity and SWC. We tested the processing steps with a synthetic study. Moreover, we used time-lapse SiMoc GPR measurements in an agricultural field to obtain SWC changes. To validate the results, the obtained permittivity and SWC values are compared with sparse single-channel multi-offset measurements and with ground truth data.

## 2 | FIELD SITE AND MEASUREMENT DESCRIPTION

The GPR measurements were conducted on an agricultural Terrestrial Environmental Observatories (TERENO) test site (Zacharias et al., 2011) in Selhausen, Germany (Figure 2a). The bare field consists of quaternary sediments covered by loess and has a 1.5% inclination in the east direction (Weihermüller et al., 2007). The climate is characterized by an average precipitation of 715 mm and a mean annual temperature of 10.2 °C (Rudolph et al., 2015). For this study, we have chosen a well-known 120-m-long transect with varying soil characteristics (Busch et al., 2014; von Hebel et al., 2014). Previous geophysical studies highlighted a lower apparent electrical conductivity ( $EC_a$ ) in the east (green line in Figure 2b), in contrast with the higher electrical conductivity in the west part of the transect (von Hebel et al., 2014). Busch et al. (2014) used the same profile for surface GPR full-waveform inversion with single-channel WARR gathers and compared the results with topsoil fractions of the obtained soil samples (0–0.3 m, Figure 2b). The west part of the transect (0 m) has stone and clay contents of 10 and 14% in the topsoil, respectively, corresponding to a lower river terrace. In the east of the profile, the stone content increases to >50%, and the clay content decreases to 7%, corresponding to the soil of the upper terrace. South of position 30 m (marked in Figure 2a), a TERENO station (Bogena, 2016) provided weather data, soil temperature, and SWC (0.05-, 0.2-, and 0.5-m depth) with a temporal resolution of 10 min. Furthermore, buried time-domain reflectometry (TDR) probes were located north of the profile (30-m position, marked in Figure 2a), providing additional SWC data (0.1-, 0.2-, and 0.3-m depth).

Ground-penetrating radar surveys were performed in November 2017, January 2018, June 2018, and October 2018 at different weather conditions and SWCs (Table 1, Figure 2c). Prior to the measurements in November 2017 and January 2018, rain events occurred, and the measurements in June and October 2018 were conducted during a dry heatwave (almost no rain in 20 wk). All GPR measurements were performed with shielded 500-MHz PulseEKKO antennas (Sensors & Software) using a time window of 50 ns, time sampling of

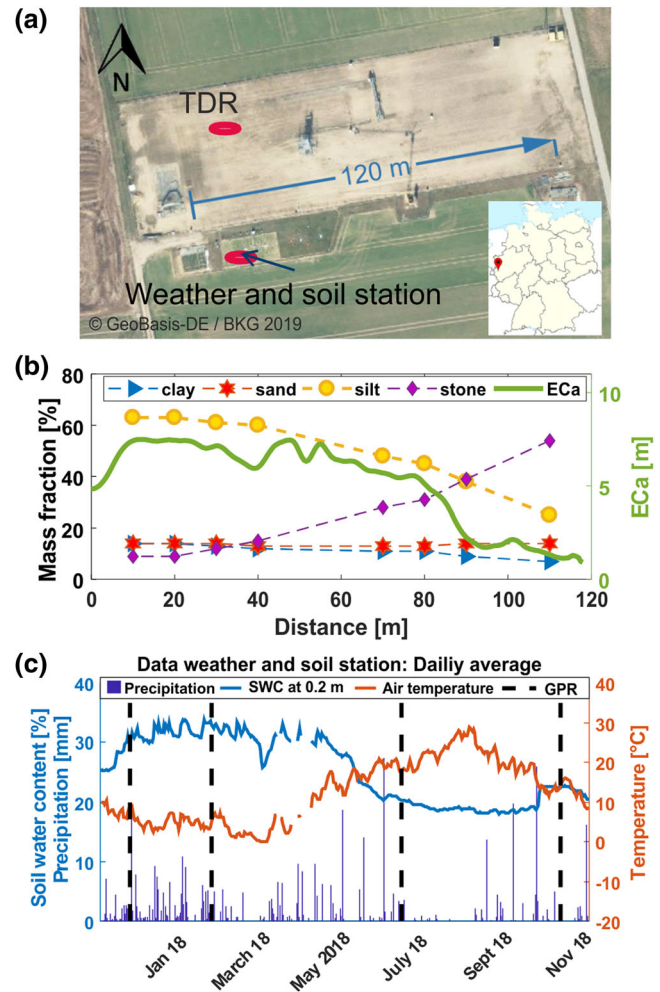


**FIGURE 2** (a) Map of the Terrestrial Environmental Observatories (TERENO) bare field in Selhausen. The blue line indicates the 120-m-long transect, and the red location shows the location of the weather station (Bogena, 2016) and time-domain reflectometry (TDR) probes. (b) Soil mass fraction after Busch et al. (2014) and apparent electrical conductivity ( $EC_a$ ) of electromagnetic induction measurement (horizontal coplanar with coil spacing of 0.3 m) after von Hebel et al. (2014). (c) Daily precipitation, air temperature, and soil water content (SWC) at 0.2 m with the black lines indicating ground-penetrating radar (GPR) measurements days

**TABLE 1** Overview of the ground-penetrating radar (GPR) measurements acquired at the Selhausen site indicating the survey parameters

Date	Single-channel WARR <sup>a</sup> GPR	SiMoc <sup>b</sup> GPR step size
		m
23 Nov. 2017	at 10 and 110	0.025
23 Jan. 2018	every 10	0.02
14 June 2018		0.05
11 Oct. 2018	every 30	0.05

<sup>a</sup>WARR, wide-angle reflection and refraction.

<sup>b</sup>SiMoc, simultaneous multi-offset multichannel.



0.2 ns, and a stack of 16. For the multi-offset measurement, the WARR-machine was used, and the 120-m-long transect was measured in <5 min. During the measurements, we ensured a constant ground coupling of the sledge. On different days, varying step sizes were used (Table 1). All data were interpolated to CMPs (0.05-m step size). For comparison, single-channel WARR measurements with a maximum offset of 5 m and a step size of 0.02 m were collected every 10 m in January 2018 and every 30 m in October 2018.

### 3 | SIMULTANEOUS MULTI-OFFSET MULTICHANNEL GROUND-PENETRATING RADAR DATA PROCESSING

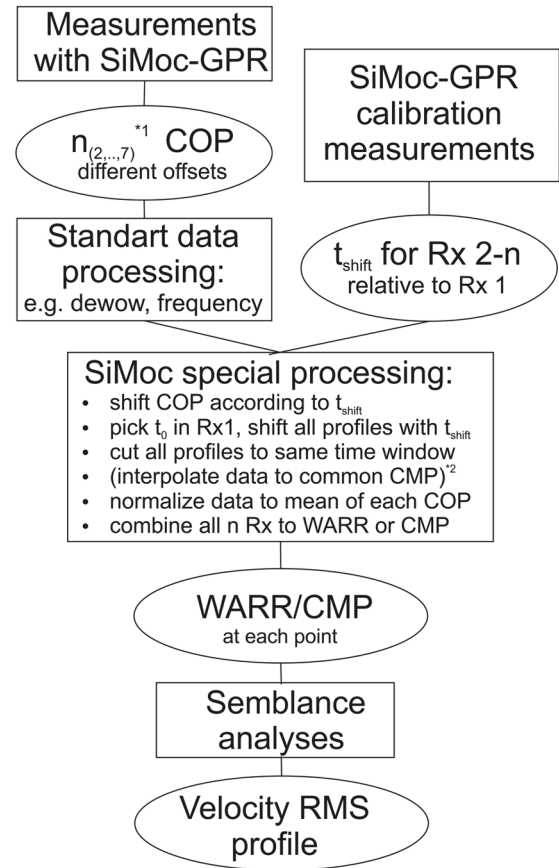
To analyze the SiMoc GPR data, processing steps similar to seismic were used (Yilmaz, 2001). The processing steps were performed in MATLAB (MathWorks) and are indicated in Figure 3. First, the up to seven COPs are separately processed using standard GPR routines: dewow filtering and, if needed (not needed on shown data), suppression of noise with a median and/or frequency bandpass filter (Jol, 2008). After a time zero correction, the seven COPs were combined with WARR or CMP gathers. In the sections below, the processing steps are explained for the January 2018 dataset in more detail.

#### 3.1 | Simultaneous multi-offset multichannel time zero calibration measurements

For GPR data, the first arrival of the received signal,  $t_0$  (red dots in Figure 4a) is often delayed, when compared with the theoretical first arrival (dashed green line) of the airwave  $t_{\text{theory}}$  at a given antenna offset (Yelf, 2004). This time difference is defined as  $t_{\text{offset}}$  (blue arrow):

$$t_{\text{offset}} = t_0 - t_{\text{theory}} \quad (1)$$

The  $t_{\text{offset}}$  are caused by the measurement equipment by a measurement time delay ensuring that the complete signal is well captured. Additionally,  $t_{\text{offset}}$  is influenced by parameters like temperature, cable length, small differences in the hardware of the antennas, and interference with other antennas, cables, and/or the sledge (Babcock, Annan, & Bradford, 2016). Therefore, each Rx has its own time delay ( $t_{\text{offset}}^{\text{Rx1-7}}$ ) compared with the theoretical first arrival of the air wave, resulting in inconsistent raw WARR gathers measured with the WARR-machine (Figure 4a). Regular  $t_0$  picking correction failed, as at smaller offsets (e.g., Rx1, Rx2), near-field effects disturb the airwave, and at larger offsets, low amplitudes and low signal-to-noise ratio hinder the correct identification of  $t_0$ , as also described by Gerhards



<sup>\*1</sup> n depends on number receivers used, maximum 7 with WARR machine

<sup>\*2</sup> automatically WARR gathers measured, for CMP gathers interpolation needed

**FIGURE 3** Processing flow for simultaneous multi-offset multichannel (SiMoc) ground-penetrating radar (GPR) data showing the process of combining common-offset profile (COP) to wide-angle reflection and refraction (WARR) or common midpoints (CMPs) gathers and the time zero correction ( $t_0$ ), by calibrating for each receiver (Rx) a separate time shift ( $t_{\text{shift}}$ ) to obtain the correct total time offset ( $t_{\text{offset}}$ ). The interpolation to CMPs is only essential when the data are rearranged to CMP gathers

et al. (2008). However, for a reliable velocity analysis, it is crucial to eliminate any relative time shift ( $t_{\text{shift}}^{\text{Rx2-7}}$ ) between the different Rxs. Therefore, we developed a novel calibration method by collecting for all seven Rxs the same dataset at one location at a field site. Thereby, the Tx was at its usual first position, and each Rx was placed at all seven slots within the sledge. As an example, Figure 4b shows the measured data for Rx1, where the linear move-out (LMO) of the airwave (red line) is clearly visible. Since the seven recorded WARRs (one for each Rx) were measured using the same offsets at the same positions, they looked very similar but are shifted in time relative to each other. To identify the correct shift relative to Rx1, the WARRs of Rx2 to Rx7 were successively shifted in time [ $t_{\text{range}}(j)$  between  $-20$  and  $20$  ns]. The obtained time-shifted WARRs are subtracted by the original WARR gather of Rx1, and the absolute mean difference  $\{\Delta\mu_{\text{RxN}[t_{\text{range}}(j)]}\}$  is

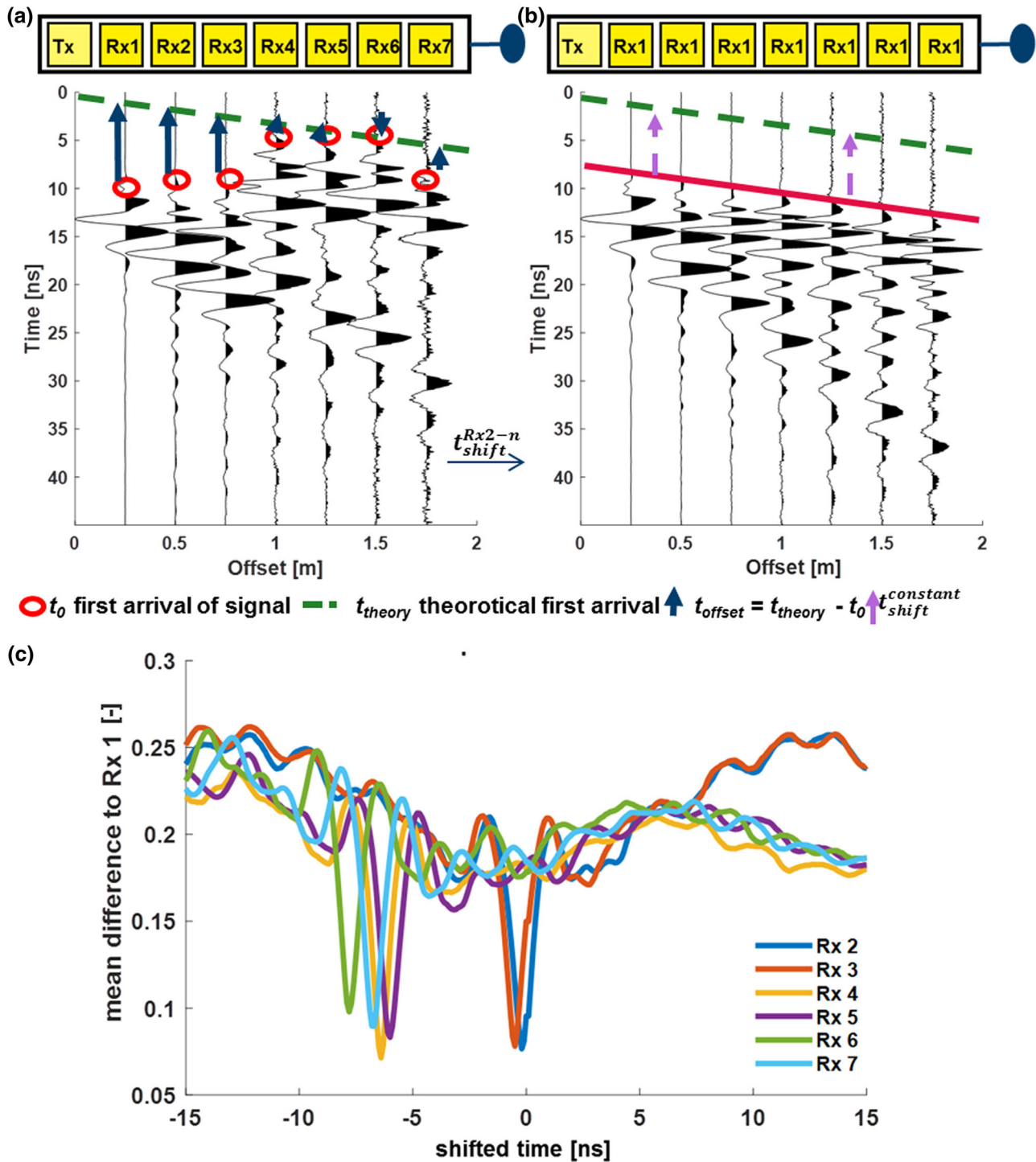


**FIGURE 4** (a) Measured raw wide-angle reflection and refraction (WARR) gather with the transmitter (Tx) and all seven receivers (Rxs) at their positions in the sledge. The red circle show the actual first arrival ( $t_0$ ) for each Rx, and the green line shows the theoretical time of the first arrival ( $t_{theory}$ ). The time discrepancy between them shows that each Rx has its own time offset ( $t_{offset}$ ). (b) WARR gather with Rx1 at all seven positions within the sledge. (c) The relative mean difference between WARR gathers of Rx2–Rx7 and WARR gather of Rx1 at time shifts within -20 and 20 ns. The smallest mean difference for each Rx indicates the correct time shift relative to Rx1 ( $t_{shift}^{Rx2-n}$ ). An additional day dependent constant shift ( $t_{shift}^{constant}$ ) equal for all seven receivers is essential for the complete time zero calibration.

calculated for each Rx and each time shift:

$$\Delta\mu_{\text{Rx}N}[t_{\text{range}}(j)] = \frac{\sum_{i=1}^{M+t_{\text{range}}(j)/\Delta t} \sum_{\text{offset}=1}^7 \left[ \begin{array}{c} \text{WARR}_{\text{Rx}N i+t_{\text{range}}(j)/\Delta t, \text{offset}} \\ -\text{WARR}_{\text{Rx}1 i, \text{offset}} \end{array} \right]}{7M} \quad (2)$$

whereas  $N$  is the Rx number,  $M$  the total number of samples, and  $\Delta t$  is the sampling rate. For each Rx, the absolute mean difference has a clear minimum related to the correct relative time shift  $t_{\text{shift}}^{\text{Rx}2-7}$  (Figure 4c). We repeated this calibration measurement 15 times at different locations and days and observed that these relative shifts of the Rxs were stable. Therefore, with the same hardware (cable, Rx), the time-consuming ( $\sim 40$  min) calibration needs to be performed once.

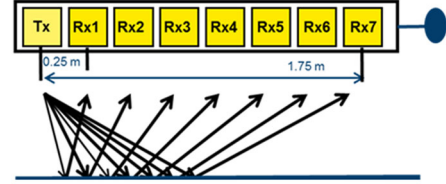
An additional constant shift ( $t_{\text{shift}}^{\text{constant}}$ ) equal for all seven Rxs, arising from different measuring delays, coupling, or temperature, needs to be determined for each field and day separately. The  $t_{\text{shift}}^{\text{constant}}$  can be picked in one of the COPs or any of the obtained WARR or CMP gathers. In total, all COPs were shifted by

$$t_{\text{offset}}^{\text{Rx}1-7} = t_{\text{shift}}^{\text{constant}} + t_{\text{shift}}^{\text{Rx}2-7n} \quad (3)$$

### 3.2 | Rearranging to wide-angle reflections and refractions and common midpoint gathers

Before rearranging the COPs to WARR and CMP gathers, all datasets must be cut to a common time window. As the amplitude with larger offsets decreases, all COPs were normalized with the absolute mean amplitude of the corresponding COP. In this way, all traces and offsets obtain similar amplitudes within one CMP or WARR gather essential for the semblance analysis. Furthermore, relative amplitude changes along transects are still traceable. The COPs were rearranged to WARR gathers using all seven traces with the same Tx position (same trace number, Figure 5a). Note that the data can also be arranged to CMP gathers by calculating for each Tx–Rx pair a CMP and sorting the data accordingly, as shown in Figure 5b. However, when the used step size is not a multiplier of 0.125 m (CMP of Tx and Rx1), the COPs are spatially interpolated to equal the CMP positions. Similar to seismic systems, both WARR and CMP gathers can be used for velocity analyses (Yilmaz, 2001). Traditionally, CMP gathers are preferred, as the semblance velocity is less sensitive for dipping layer structures (Yilmaz, 2001). Therefore, we analyzed the data with CMP gathers rather than WARR gathers.

#### (a) Schematic sketch of automatically measured WARR



#### (b) Schematic sketch of rearranged CMP gather

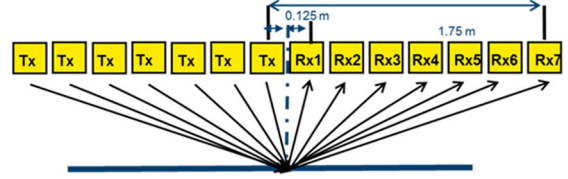


**FIGURE 5** Schematic sketch of the position of transmitter (Tx) and receivers (Rx) (a) at an automatically measured wide-angle reflection and refraction (WARR) and (b) for rearranged data with common midpoints (CMPs)

### 3.3 | Semblance

Velocity analyses were performed with a combined LMO and hyperbolic move-out (HMO) semblance approach (Dal Bo et al., 2019), as shown exemplarily in Figure 6. As the ground wave (direct wave) is a linear event traveling through the upper centimeters of the subsurface, LMO was calculated for the first nine nanoseconds (in plot, only 4 ns is shown). Whereas reflections cause HMOs in multi-offset gathers, HMO calculations were applied for later times. The semblance coefficient is a normalized coherency along a linear or hyperbolic travel path in a WARR or CMP gather. This coefficient is calculated at each zero-offset time, considering a time window similar to the pulse width for a given velocity range (Heincke, Green, Van Der Kruk, & Willenberg, 2006). A good velocity fit returns a high semblance coefficient value, and after normal move-out (NMO), events align horizontally (Luo & Hale, 2012). The velocities are determined by manually picking semblance maxima corresponding to events in a gather. Each pick was confirmed with a superimposed line or reflection on the gather and an NMO correction image. Additionally, in each semblance, the time  $t_{\text{end}}$  with the last semblance coefficient value  $> 0.4$  [–] was determined. This  $t_{\text{end}}$  corresponds to the last coherent signal at zero offset.

#### 3.3.1 | Synthetic study: Interference groundwave and reflection

We performed a simple synthetic study to estimate the accuracy of retrieved soil velocities (or permittivity) and layer depths obtained by the semblance analysis. We defined a 3D model ( $x = 7$  m,  $y = 7$  m,  $z = 0.2$  m) with two horizontal soil layers and an air layer on top. For each model, we computed

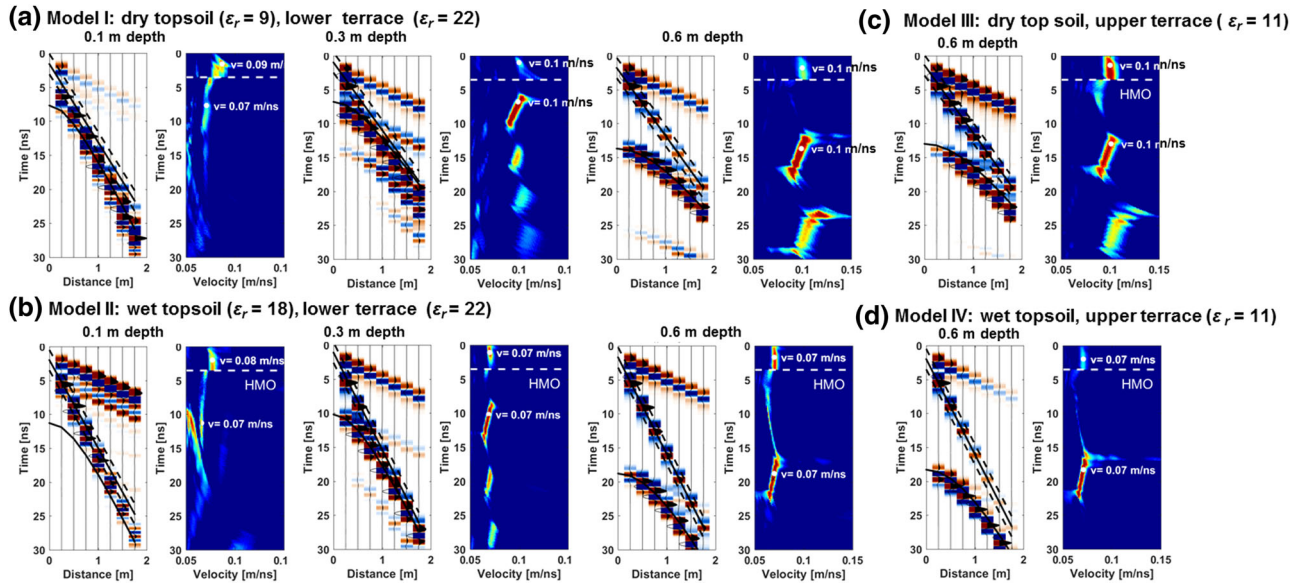


**FIGURE 6** Synthetic two-layer studies with varying depth of the topsoil created with gprMax. For Models I–IV (different dielectric permittivity,  $\epsilon_r$ ), the common midpoint (CMP) and wide-angle reflection and refraction (WARR) gathers, and their corresponding combined linear and hyperbolic moveout semblance is shown. The white line separates linear move-out (LMO) and hyperbolic move-out (HMO) semblance panels. The white circles indicate the picked velocities ( $v$ ) and time of the ground wave and reflection. The corresponding wave is plotted in the WARR and CMP gathers. On the groundwave, the dashed lines are indicating the width of the time window used in the semblance calculation

the electromagnetic waves using the 3D finite difference time domain solver gprMax (Warren, Giannopoulos, & Giannakis, 2016). The model parameters were chosen to represent the Selhausen test site (west and east part of the transect, called lower and upper terrace). Therefore, two different models with different subsoils (second layer) were used, one similar to the lower terrace ( $\epsilon_r = 22$ ,  $\sigma = 30 \text{ mS m}^{-1}$ ) and one similar to the upper terrace ( $\epsilon_r = 11$ ,  $\sigma = 10 \text{ mS m}^{-1}$ ). To test the impact of dry and wet soil on the groundwave velocity estimation, additionally, two different topsoils (first layer) were used ( $\epsilon_r = 9$  for dry soil and  $\epsilon_r = 18$  for wet soil). Synthetic WARR or CMP gathers with WARR-machine offsets (seven traces) were calculated for each of these four scenarios:

- Model I: dry topsoil on top of subsoil representing lower terrace of Selhausen
- Model II: wet topsoil on top of subsoil representing the lower terrace of Selhausen
- Model III: dry topsoil on top of subsoil representing upper terrace of Selhausen
- Model IV: wet topsoil on top of subsoil representing upper terrace of Selhausen

Additionally, for each model type, seven models with different topsoil thickness of 0.1 and 0.7 m were created. In the resulting 28 WARR or CMP gathers and their corresponding semblance, the groundwave and reflection were picked, and the depth of the first layer was calculated (see Figure 6 and Table 2). Except for the gathers with the two thinnest first

layer thickness (0.1 and 0.2 m), the semblance results agree with the model within  $0.01 \text{ m ns}^{-1}$  and 0.02 m for velocities and layer depth, respectively. As expected, the second-layer properties do not affect the semblance results. However, for models with larger permittivity changes (Models I and IV, Figures 6a and 6d) and therefore higher absolute reflection coefficient, the amplitude of the groundwave is weaker in the gather and semblance. Additionally, in Model IV, the reflection coefficient is negative, resulting in a phase change at the reflection (no effect in semblance).

For models with the thinnest first-layer thickness (0.1 and 0.2 m), groundwave and reflection interfere in WARR or CMP gathers (Figures 6a and 6c). With increasing thickness, the reflection and groundwave are separated (for thinner layers only at smaller antenna offsets). For dry conditions (larger velocity), groundwave and reflection interfere at later times. Furthermore, in models with shallow layers, groundwave and reflection velocity differ. This might be explained by a larger sensing depth of the groundwave than the thickness of the first layer. Therefore, the groundwave velocity is partly affected by the second layer. Due to the interference of groundwave and reflection, the exact sampling depth of the groundwave cannot be estimated. Also, other studies (Galagedara, Redman, Parkin, Annan, & Endres, 2005; van Overmeeren et al., 1997) conclude that the sampling depth of the groundwave is hard to determine and depends on various parameters (e.g., frequency, offsets, soil, and wet or dry condition). Generally, the sampling depth increases with larger offsets and decreases with increasing SWC.



**TABLE 2** Overview of the parameters of the synthetic study and obtained velocity ( $v$ ) and layer depth ( $d$ )

Topsoil thickness m	Lower terrace ( $\epsilon_r^a = 22$ , $\sigma^b = 30 \text{ mS m}^{-1}$ )						Upper terrace ( $\epsilon_r = 11$ , $\sigma = 10 \text{ mS m}^{-1}$ )					
	Model (dry $\epsilon_r = 9$ , $v = 0.1 \text{ m ns}^{-1}$ )			Model II (wet $\epsilon_r = 18$ , $v = 0.07 \text{ m ns}^{-1}$ )			Model III (dry $\epsilon_r = 9$ , $v = 0.1 \text{ m ns}^{-1}$ )			Model IV (wet $\epsilon_r = 18$ , $v = 0.07 \text{ m ns}^{-1}$ )		
	$v$	GW <sup>c</sup>	Ref <sup>d</sup>	$d$	Error in $d$	Error in $v$	$v$	GW	Ref	$d$	Error in $d$	Error in $v$
	m	m	m	m	m	m	m	m	m	m	m	m
0.1	0.068	0.098	0.328	0.228	0.077	0.066	0.323	0.223	0.113	0.081	0.22	-0.12
0.2	0.107	0.098	0.181	-0.019	0.073	0.069	0.193	-0.007	0.107	0.096	0.2	0.00
0.3	0.100	0.099	0.272	-0.028	0.070	0.069	0.300	0.000	0.100	0.098	0.28	0.02
0.4	0.097	0.100	0.380	-0.020	0.071	0.070	0.389	-0.012	0.099	0.099	0.38	0.02
0.5	0.100	0.100	0.480	-0.020	0.070	0.071	0.483	-0.017	0.100	0.100	0.48	0.02
0.6	0.100	0.099	0.604	0.004	0.070	0.070	0.606	0.006	0.100	0.101	0.58	0.02
0.7	0.100	0.100	0.700	0.000	0.070	0.071	0.689	-0.011	0.100	0.102	0.69	0.01

<sup>a</sup> $\epsilon_r$ , dielectric permittivity.<sup>b</sup> $\sigma$ , electrical conductivity.<sup>c</sup>GW, groundwave.<sup>d</sup>Ref, reference.

### 3.3.2 | Automatic groundwave velocity picking with filtering

With a large number of WARR or CMP gathers ( $\sim 2,000$  gathers for 100 m), manual picking is time consuming. Therefore, an automatic picking routine was implemented. The ground wave velocity was obtained by automatically determining the maximum in the LMO semblance within a predefined velocity interval (here,  $0.05\text{--}0.15 \text{ m ns}^{-1}$ ) within the first 8 ns. By considering the entire pulse width of the signal, the maximum of the groundwave was not at 0 ns. Time variation of the groundwave LMO semblance maximum might be caused by near-field effects and by interference with the airwave. Velocity outliers were removed with a filtering routine (shown as an example in Figure 7). Firstly, velocity picks with 30% lower semblance coefficients than the mean picked semblance coefficient over the profile were disregarded (threshold is shown with a dashed line in Figure 7b). These criteria filter out noisy WARR or CMP gathers where no clear groundwave was visible (low and blurred semblance maxima). Secondly, picks at the upper and the lower bound of the selection window were excluded. These picks were often due to either airwave or shallow reflection interference. In general, with this simple filtering method, automatic picking returned realistic ground wave velocities (compared with manual picking) but is not influenced by subjective decisions or picking errors and is more quickly obtained.

As reflections vary in numbers and depths along the profile, the automatic search of maxima within predefined time intervals in HMO failed to recover maxima corresponding to hyperbolic events in the CMP or WARR gathers. Further studies or manual adaption of the time interval are necessary. In our studies, we used a semiautomatic approach. For each WARR or CMP gather, areas with maxima in the HMO semblance were manually selected. Around these areas, the true maxima were automatically searched. This automatic search saves time (hard to locate maximum manually) and guarantees partial objectiveness by constantly picking the true maximum.

## 4 | RESULTS OF GROUND-PENETRATING RADAR MEASUREMENTS

### 4.1 | Common-offset profiles

Figure 8 shows the profiles measured in January 2018 of Rx1 and Rx7 for 0.25- and 1.75-m offsets, respectively. Note that the amplitudes of Rx7 were a factor of 10 smaller than those of Rx1. The ground wave (dashed green line) was visible in the Rx7 data, whereas it interfered with the airwave for Rx1 due to the small offset. Along the GPR profile between 100 and

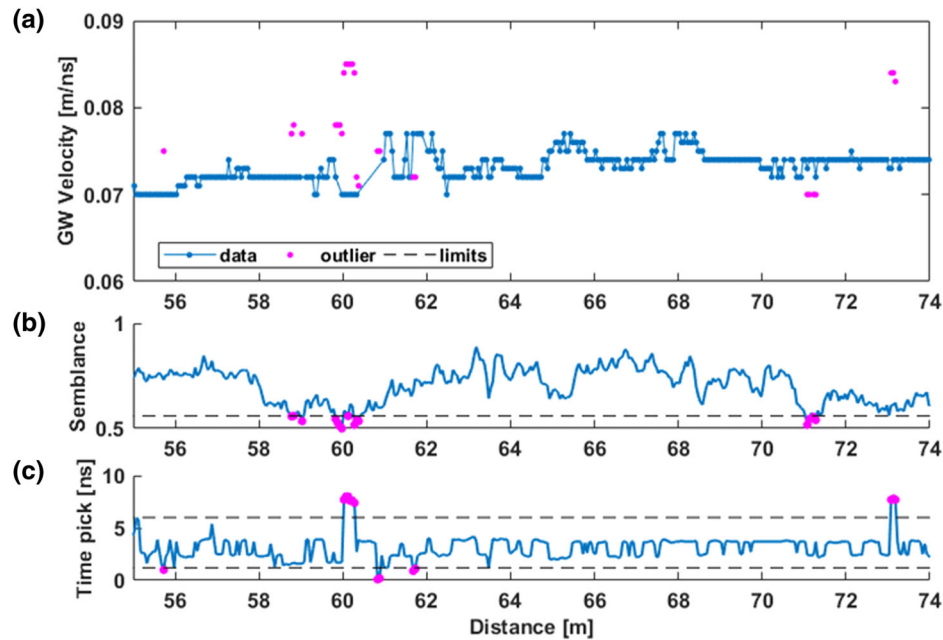


**FIGURE 7** Filtering of the automatically picked ground wave shown as an example between 55 and 74 m. (a) Groundwave (GW) velocity, (b) corresponding semblance amplitude, and (c) picked semblance time. The pink dots correspond to deleted outliers, due to low amplitude ( $<30\%$  of mean amplitude) or time picks outside a selected interval (here, 1–6 ns)

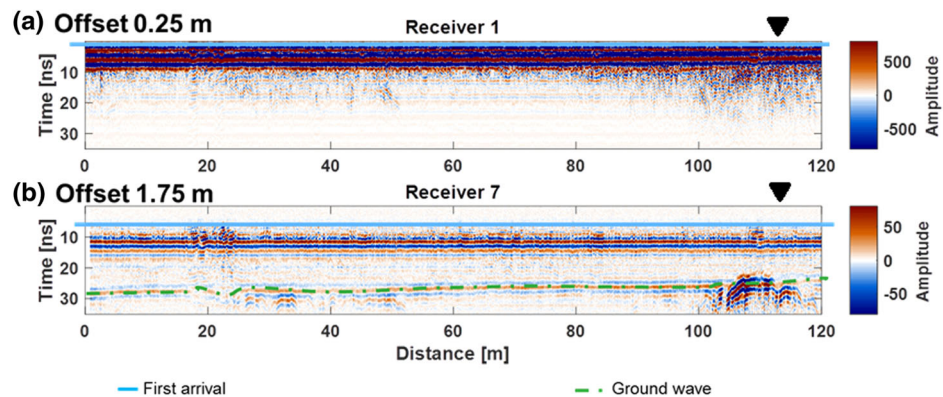


**FIGURE 8** Common-offset profile (COP) measured in January 2018 (a) for Receiver 1 with an offset of 0.25 m and (b) for Receiver 7 with an offset of 1.75 m. In both profiles, the first arrival of the airwave is indicated by a blue line. In Panel b, the dashed green line indicates the ground wave, whereas in Panel a, the ground wave interferes with the airwave. The position of the wide-angle reflection and refraction (WARR) gathers of Figure 9 is indicated by a triangle

120 m, a heterogeneous area with late-arriving higher amplitudes can be observed related to a low conductive zone in the EMI data (von Hebel et al., 2014). The two heterogeneous GPR reflection patterns around 20 m are caused by tire tracks.

#### 4.2 | Comparison of simultaneous multi-offset multichannel ground-penetrating radar data with single-channel data

The SiMoc GPR data was compared with single-channel data and are shown as an example at location 115 m of the profile

(Figure 9). The spatially sampled (offset sampling of 2 cm) single-channel WARR (Figure 9a) was downsampled to seven traces with the same offsets as SiMoc GPR (Figure 9b) and compared with SiMoc WARR (Figure 9c), and SiMoc CMP gathers (Figure 9d). In the dense single-channel WARR gather, the airwave, groundwave, and one reflection can be recognized (Figure 9a). Except for the airwave (interference with a sledge and other Rxs), SiMoc WARR and CMP gathers (Figures 9c and 9d) were very similar to the single-channel data. In all semblances, a clear maximum for a ground wave velocity of  $0.07 \text{ m ns}^{-1}$  was observed, whereas

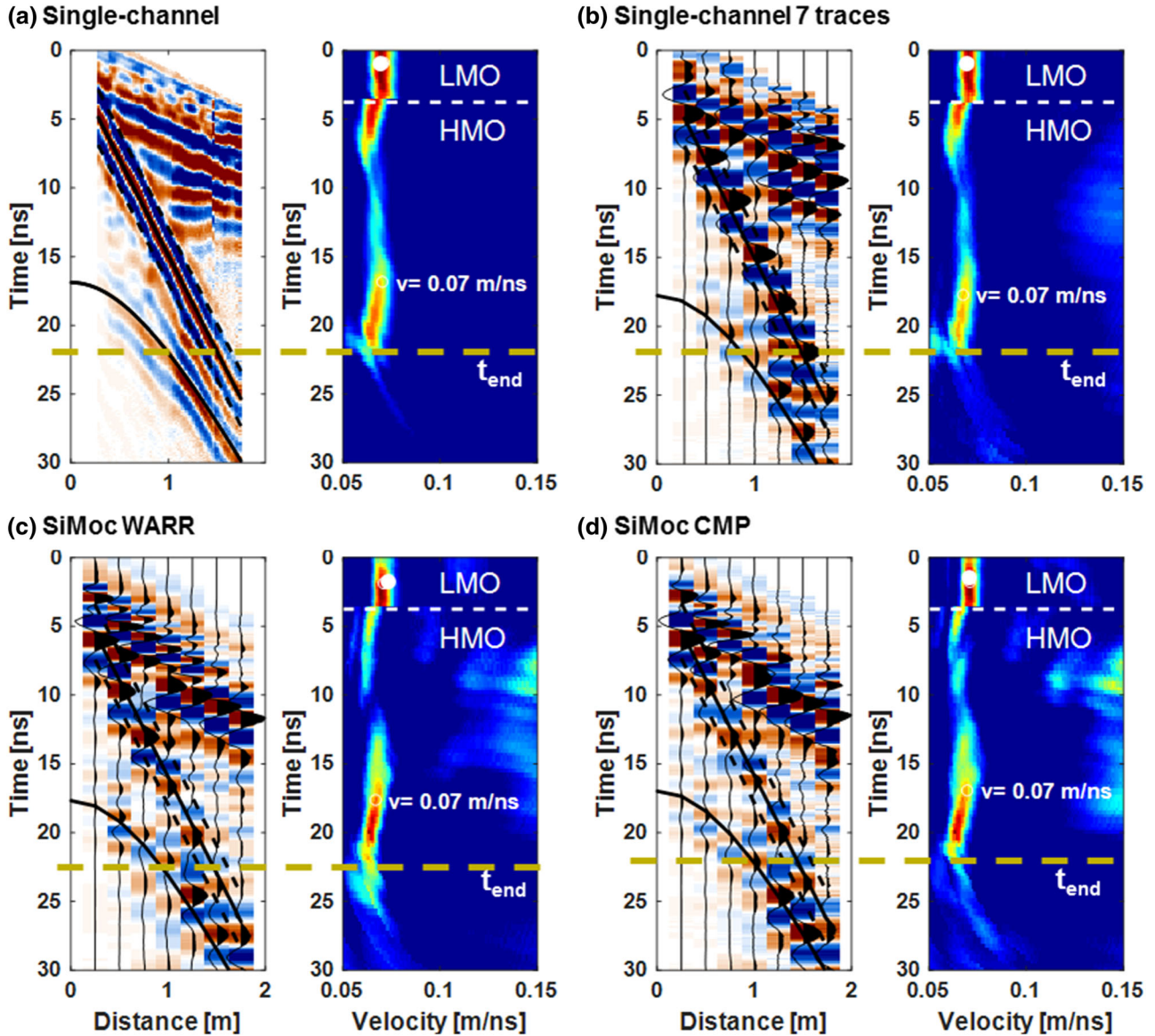


**FIGURE 9** Comparison of (a–b) single-channel and (c–d) simultaneous multi-offset multichannel (SiMoc) ground-penetrating radar (GPR) measurements at position 115 m (marked with a triangle in Figure 8). For comparison, the single-channel wide-angle reflection and refraction (WARR) in Panel a was downsampled to seven traces (Panel b) with the same offsets as SiMoc GPR. For all (a–c) WARR and common midpoint (CMP) gathers, the corresponding combined linear (LMO) and hyperbolic move-out (HMO) semblance with a line separating LMO and HMO semblance panels are shown. The white circles indicate the picked velocities ( $v$ ) of the groundwave and reflection, corresponding to the black lines in the WARR and CMP gathers. On the groundwave, the dashed lines are indicating the width of the time window used in the semblance calculation. The gold lines mark  $t_{\text{end}}$ , the last time with higher semblance amplitude than 0.4 and thus coherent signal

reflection semblance maxima were obtained for velocities around  $0.07 \text{ m ns}^{-1}$  between 17 and 22 ns. This comparison demonstrates that SiMoc data with seven traces is comparable with common single-channel WARR and can be used to produce reliable velocity estimates. As measuring a normal single-channel WARR is time consuming and limited to point scale, the SiMoc GPR offers a unique possibility to gather fast and uncomplicated velocity and permittivity estimates.

### 4.3 | Velocity along profile

For the January datasets, we compared the ground wave velocity derived with different methods (Figure 10): manually picking the groundwave in COPs of Rx3, Rx5, and Rx7 (blue), and a semblance approach with single-channel WARR (every 10 m) and SiMoc data with manual picking (every 0.50 m, on WARR gathers) and automatic picking (every 0.05 m, on WARR and CMP gathers). Overall, a general trend of



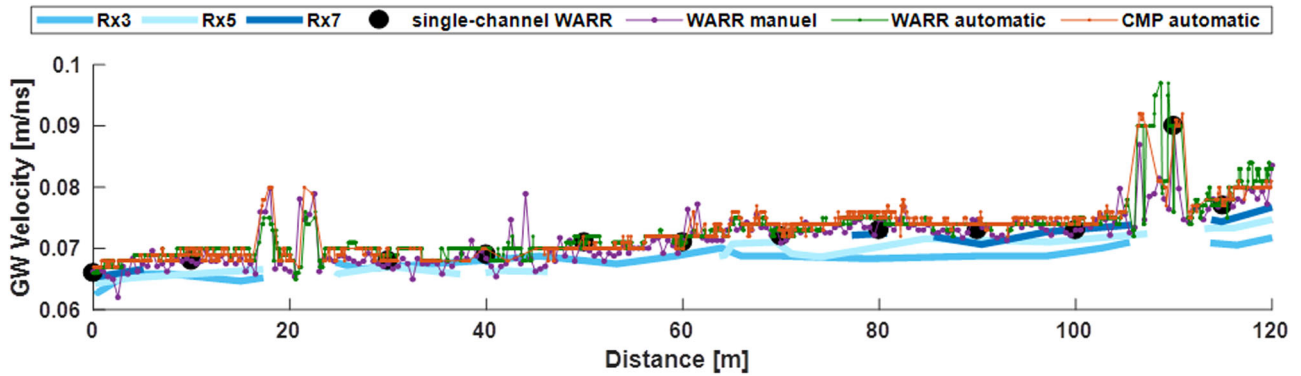


**FIGURE 10** Comparison of the groundwave (GW) velocities obtained with different methods along the profile in January 2018: single-channel GW picking in common-offset profile of Receivers (RXs) 3, 5, and 7 (blue), single-channel wide-angle reflection and refraction (WARR, black dot), and with simultaneous multi-offset multichannel (SiMoc) ground-penetrating radar (GPR); manual picked WARRs (purple); and automatically picked WARR (green) and common midpoint (CMP, red)

increasing ground wave velocity from the west ( $0.065 \text{ m ns}^{-1}$ ) to the east ( $0.08 \text{ m ns}^{-1}$ ) was present. The ground wave velocities obtained in COP were lower than the semblance-approach-derived velocities (especially in the east, higher velocity). By handpicking the ground wave in COPs, the velocity is highly dependent on accurate travel time picks (Huisman et al., 2003). Furthermore, the groundwave was not completely recognizable along the profile in any of the COPs (antenna separation =  $0.25\text{--}1.75 \text{ m}$ ). Whereas with smaller antenna separation (e.g., Rx 3) groundwave and airwave interfered more strongly in the east (larger  $v$ ), with larger antenna separation (e.g., Rx 7), the groundwave was weak.

The groundwave velocity derived with semblance agreed (within  $0.001 \text{ m ns}^{-1}$ ) with single-channel GPR WARR gathers. All SiMoc data returned similar ground wave velocities (mean absolute difference  $< 0.002 \text{ m ns}^{-1}$ ). The greatest differences were observed at locations where reflections and groundwave interfere (around 40 and 110 m). However, due to the near-surface reflections and diffractions at these locations, COP picking and single-channel WARR gathers also returned no reliable ground wave velocity, as shown in the synthetic study.

The main advantage of SiMoc GPR is the high amount of data availability, so the groundwave velocity can be derived by either picking the groundwave in COPs without determining a suitable antenna separation beforehand or with a semblance approach. The semblance approach is less affected by travel time picks and is fully automated.

Furthermore, by plotting LMO and HMO semblance results together, a velocity cross-section vs. time can be created (e.g., with the January 2018 dataset and semiautomatized picks every  $0.5 \text{ m}$ ; Figure 11a). The HMO semblance velocities correspond to average velocities  $v_{\text{RMS}}$  from the surface to picked zero-offset time (Yilmaz, 2001). Filtered or velocities deeper than  $t_{\text{end}}$  were ignored (blank in Figures 11a and 11b). Additionally, the average velocity ( $v_{\text{RMS}}$ ) was

transferred to interval velocity  $v_{\text{int}}$  using the Dix formula (Dix, 1955), and actual layer thicknesses were determined.

## 5 | SOIL CHARACTERIZATION USING TIME-LAPSE GROUND-PENETRATING RADAR DATA

### 5.1 | Permittivity profile

For soil characterization, the interval velocity profile was transferred to  $2\text{D } \epsilon_r$  vs. depth profiles with

$$\epsilon_r = \left( \frac{c_0}{v_{\text{int}}} \right)^2 \quad (4)$$

where  $c_0$  is the velocity in the air. The permittivity depth profile is comparable with the EMI inversion results (Figure 11c, after von Hebel et al., 2014). For example, in January 2018, the topsoil permittivity decreased from west to east (Figure 11b), in correspondence with a conductivity decrease in the first layer of the inverted EMI data. These changes of  $\epsilon_r$  and conductivity can be linked to soil texture changes from silty loam to gravel-rich soil (Figure 2b). Furthermore, the shallow recorded depth and the fast attenuation of the GPR signal in the first 80 m can be explained by high conductivities in the EMI data. Additionally, on the lower terrace ( $0\text{--}100 \text{ m}$ ),  $\epsilon_r$  increased with depth (when reflection present), consistent with assumed higher SWC with depth (e.g., Fisher et al., 1992). However, in the east ( $100\text{--}120 \text{ m}$ ), the permittivity decreased with depth, indicating a texture change.

Whereas the results of SiMoc GPR correspond to directly measured information of soil layers with different  $\epsilon_r$  (Jol, 2008), the EMI data are sensitive to  $\sigma$  changes, and layer thickness and depth are only obtained with inversion techniques



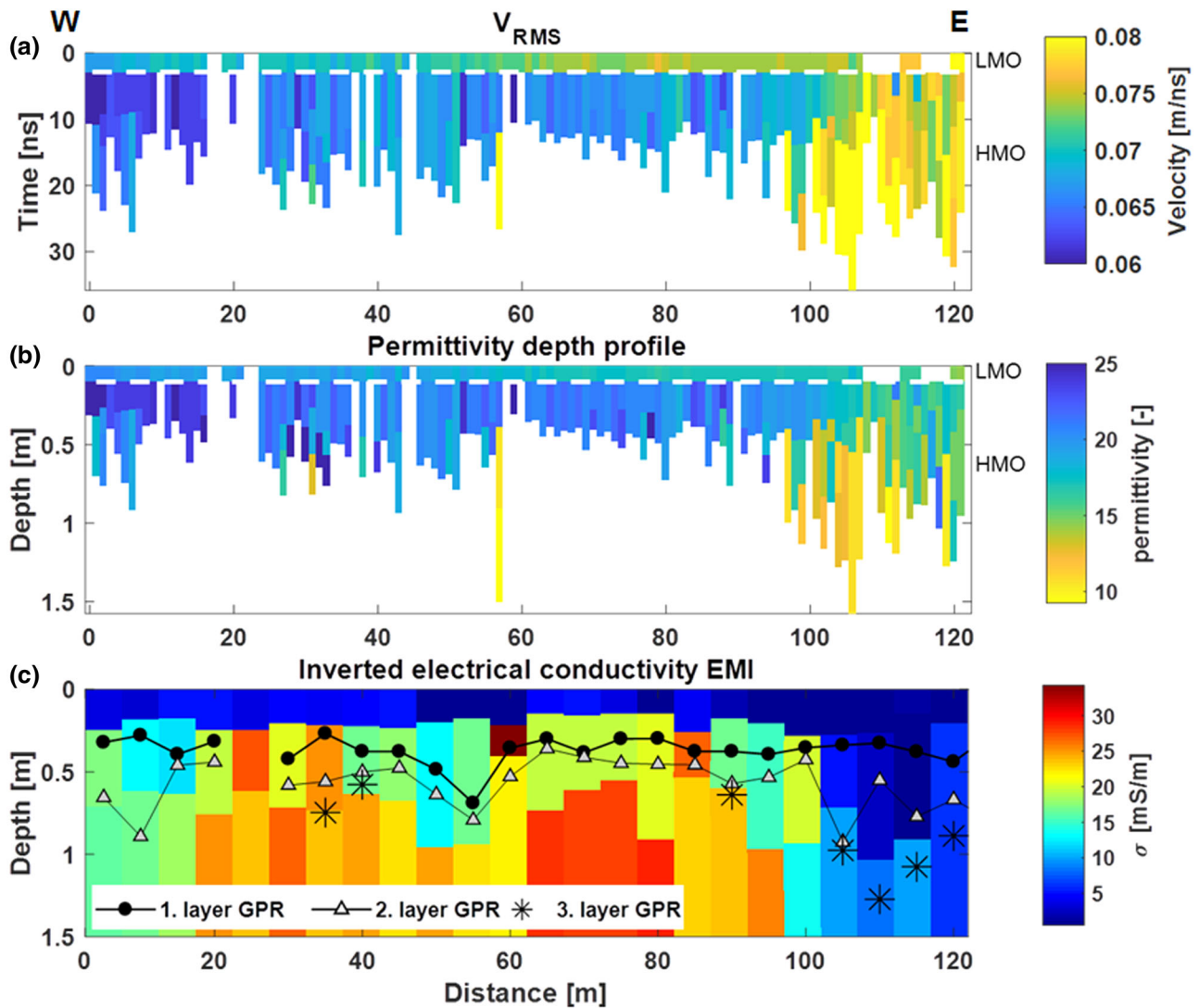


**FIGURE 11** (a) Velocities profile from semblance resembling average velocity ( $v_{\text{RMS}}$ ) from west (W) to east (E). The groundwave velocities picked in the linear move-out (LMO) is plotted above the white line, and the filtered groundwave appears white. Below the reflection velocities picked in hyperbolic move-out (HMO) are plotted with their corresponding time. White space below corresponds to times later than any events in the data. (b) Permittivity profile vs. depth obtained from interval velocities with groundwave permittivity on top. (c) For comparison, the depth of the ground-penetrating radar (GPR) layers (black) over the inverted electrical conductivity measured with electromagnetic induction (EMI) according to von Hebel et al. (2014)

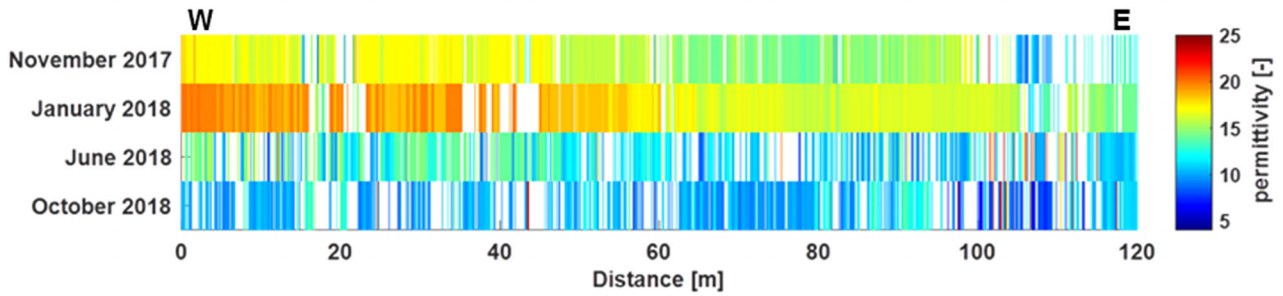
(von Hebel et al., 2019). For a better comparison of both methods, the layer depths obtained by SiMoc GPR (averaged by 5 m) are plotted over the EMI inversion results (Figure 11c). In both methods, the first layer is consistent across the profile and is probably indicating the plough horizon. The depths of the EMI and GPR layer are different by 10 cm, as they were not measured on the same day (different soil conditions). In particular, the first layer of SiMoc GPR might be influenced by the wetting front (Mangel, Moysey, Ryan, & Tarbutton, 2012) after rain events. The third layer in the EMI inversion starts at 5–10 m, 25–40 m, 45–80 m, and 80–120 m at a similar depth, then a SiMoc-GPR layer boundary, indicating a soil changes in  $\epsilon_r$  and  $\sigma$ . These results show that SiMoc

GPR can be used to characterize the soil at different depths, especially in combination with EMI. Moreover, the inversion of accurate and quantitative EMI data (von Hebel et al., 2019) may be improved when guiding the layer boundaries in the EMI inversion process toward the depths inferred by GPR.

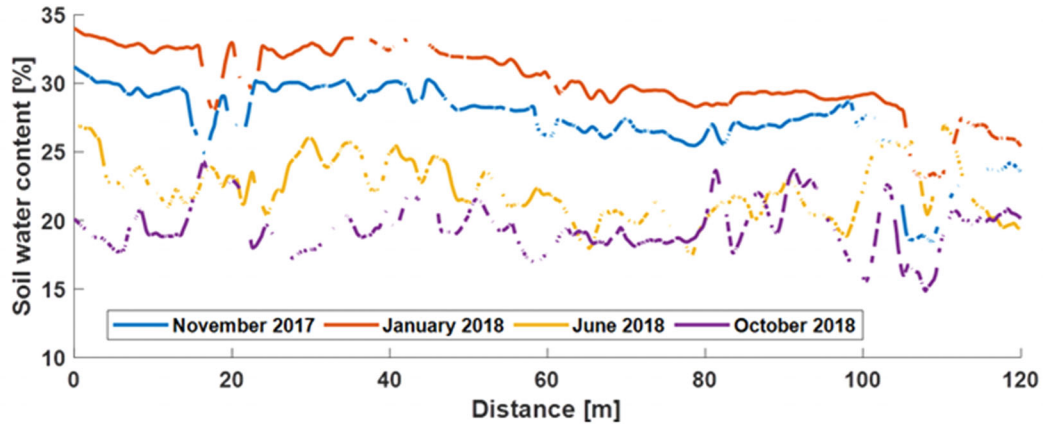
## 5.2 | Time-lapse data and soil water content

To detect permittivity changes, and hence SWC changes over time, the groundwave velocities of all four time-lapse measurements were automatically picked, and the corresponding permittivity along the profile was calculated (Figure 12a). For

## (a) Time lapse permittivity



## (b) Temperature corrected soil water content



## (c) Mean relative difference along profile

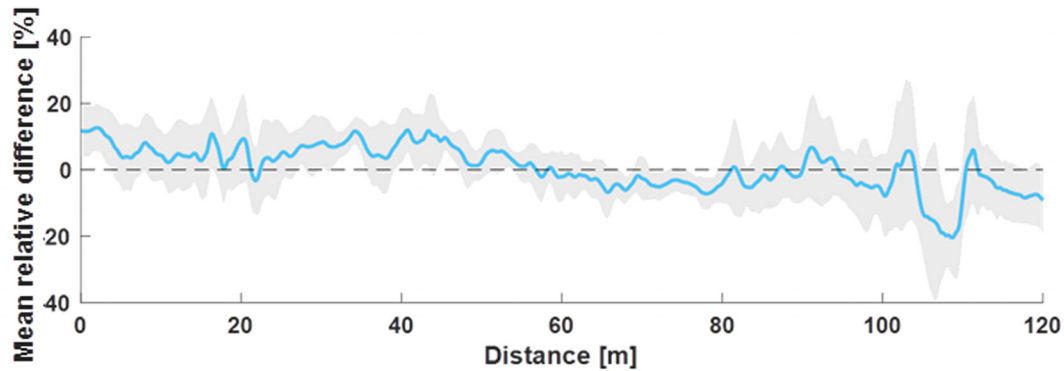


**FIGURE 12** (a) Time-lapse permittivity from west (W) to east (E), where outliers filtered out with the described methods are shown as blanks. (b) Temperature corrected soil water content, calculated using Topp's equation. To account for lateral variations within one common midpoint measurement, the soil water content is smoothed over a width of 1 m. (c) Mean relative difference of soil water content along profile with the relative difference in the standard deviation of the mean at each location calculated according to Vachaud et al. (1985)

all four dates,  $\epsilon_r$  decreased from west to east (less pronounced in October 2018), consistent with the soil texture changes. The permittivities were the highest in January 2018, with similar values in November 2017, and decreased significantly in June 2018 and October 2018. These results are consistent with weather data (Figure 2c), as the low  $\epsilon_r$  in June and October 2018 were measured during a dry heatwave. These datasets (June and October 2018) contained more outliers (blanks). Similar to Grote, Hubbard, and Rubin (2003) and the synthetic study, in the dry soils (low  $\epsilon_r$ ), groundwave

and airwave also interfere at greater offsets. Therefore, in the dry datasets, the groundwave was hardly recognizable within the COPs (different antenna separations) and CMP gathers. Nevertheless, with the automatized and filtered semblance approach, consistent groundwave velocities were obtained.

For calculating the volumetric SWC ( $\theta$ ), Topp's equation (Topp et al., 1980) was used:

$$\theta = 4.3 \times 10^{-6} \epsilon_r^3 - 5.5 \times 10^{-4} \epsilon_r^2 + 2.92 \times 10^{-2} \epsilon_r - 5.3 \times 10^{-2} \quad (5)$$

**TABLE 3** Overview of the by simultaneous multi-offset multichannel (SiMoc) ground-penetrating radar (GPR) acquired soil water content (SWC) for all four dates (along the complete profile and at 25–35 m, corresponding to the soil closest to the weather station and time-domain reflectometry [TDR] probes). Moreover, an overview of the ground truth SWC of the weather station and TDR for different depths is shown

Date	GPR mean SWC		Weather station SWC			TDR probes SWC		
	Along profile	25–35 m	0.05-m depth	0.2-m depth	0.5-m depth	0.1-m depth	0.2-m depth	0.3-m depth
	%							
23 Nov. 2017	28.0 ± 2.5	29.0 ± 1.0	31.0 ± 0.5	29.5 ± 2.7	27.0 ± 0.5	27.5 ± 0.1	28.0 ± 0.1	27.5 ± 0.1
23 Jan. 2018	30.5 ± 2.5	32.5 ± 1.0	35.0 ± 1.0	33.0 ± 3.6	32.0 ± 1.5	32.0 ± 0.1	29.0 ± 0.1	28.5 ± 0.1
14 June 2018	22.5 ± 2.5	24.4 ± 1.5	17.0 ± 3.6	20.5 ± 5.0	27.0 ± 1.0	23.5 ± 0.1	25.5 ± 0.1	23.5 ± 0.1
11 Oct. 2018	19.5 ± 2.5	18.5 ± 2.0	23.0 ± 3.0	22.5 ± 2.6	25.0 ± 1.0	21.5 ± 0.1	25.0 ± 0.1	18.5 ± 0.1

The SWC were temperature corrected with the empirical formula after Gong, Cao, and Sun (2003):

$$\theta^{20^\circ} = \frac{\theta^T - 0.008T + 0.0183}{1.075 - 0.003T} \quad (6)$$

where  $\theta^T$  is the SWC at the soil temperature  $T$  (soil station) and  $\theta^{20^\circ}$  is the corrected SWC at 20 °C. Additionally, as neighboring WARR and CMP gathers measured overlapping soil volumes, the SWCs were smoothed over 1 m (Figure 10b).

The mean SWCs obtained were 28, 30.5, 22.5, and 19.5% for November 2017, January, June, and October 2018. The SWC followed the trend of the SWC changes at the weather station and TDR probes at 0.20-m depth (Table 3 for an overview). However, the SWC difference (up to 5%) between the weather station and TDR probes shows the importance of measuring SWC with a high spatial resolution. The higher SWC in the GPR data in June than in October (different to the weather station) might be explained by a deeper sampling depth of the groundwave in dry condition. Therefore, in June, the groundwave velocity might be influenced by the wet soil below 0.2 m (as seen in the synthetic study). Over the drought in summer 2018, the deeper soil dried out, resulting in a lower SWC obtained by SiMoc GPR in October than in June.

To find different drying patterns of SWC, the temporal stability is calculated after Vachaud, Passerat de Silans, Balabanis, and Vauclin (1985). For each point along the profile, the mean relative difference of SWC and its standard deviation was calculated (Figure 12c). In the first 50 m of the profile, the SWC was in general higher than the mean SWC of a measurement day, consistent with the silty loam of the lower terrace. The general lower SWC in the east might be additionally explained with a deeper groundwater table in the upper terrace (Bogena, 2016). From 80 to 120 m, the standard deviation of the relative differences was highest; therefore, in the upper terrace, the SWC varied most over the different measurement days, which can be explained by the high stone content similar to Zhu, Shao, and Liang (2018).

## 6 | CONCLUSION

With this new SiMoc GPR system, with the same speed as common single-channel GPR, acquisition of WARR and CMP gathers and COPs are possible at the same time. We have shown that measuring seven different offsets (traces) contains sufficient information to perform a reliable velocity analysis, and we validated the results with a synthetic study, point-scale single-channel GPR WARR measurements, and ground truth soil data. We successfully developed a processing tool and provided a method for correcting the time shifts occurring at the different Rx's. Therefore with SiMoc GPR, velocity, and soil permittivity can now be obtained with a high spatial resolution. For soil characterization, 2D permittivity profiles vs. depth can be obtained, or SWC changes can be monitored. All obtained data were in agreement with soil truth data and EMI data, but compared with fixed buried sensors, field-scale variation in SWC and different drying patterns can be measured. Furthermore, additional processing steps similar to seismic data could be used. For example, on profiles with more profound reflections, the COP can be stacked to one zero-offset profile with an increased signal-to-noise ratio, and migration techniques with 2D velocity profiles could improve the final results. Finally, with an automatic determination of reflection velocity, a highly resolved 3D permittivity model at the field scale can be obtained.

## CONFLICT OF INTEREST


The authors declare no conflict of interest.

## ACKNOWLEDGMENTS

We acknowledge BMBF “BONARES,” project Soil<sup>3</sup> (Grant 031B0026C). In addition, support was received through the “Terrestrial ENvironmental Observatories” (TERENO), Advanced Remote Sensing Ground-Truth Demo and Test Facilities (ACROSS), and Transregional Collaborative Research Center 32—Patterns in Soil–Vegetation–Atmosphere Systems: Monitoring, Modelling and Data Assimilation. We thank Peter Annan and his team at Sensors & Software for developing the WARR-machine, and

especially Steven Jackson for helping to set up the system. We would like to thank Katharina Schlüter, Durra Handri Saputera, Carlos Ocampo, Jessica Schmäck, and Michael Iwanowitsch for help in the field. Additionally, we thank the anonymous reviewers and Ute Wollschläger for significantly improving the manuscript.

## ORCID

Manuela Sarah Kaufmann 

<https://orcid.org/0000-0003-3060-7375>

Anja Klotzsche  <https://orcid.org/0000-0002-7021-5045>

Harry Vereecken  <https://orcid.org/0000-0002-8051-8517>

## REFERENCES

- Adamchuk, V. I., Hummel, J. W., Morgan, M. T., & Upadhyaya, S. K. (2004). On-the-go soil sensors for precision agriculture. *Computers and Electronics in Agriculture*, 44, 71–91. <https://doi.org/10.1016/j.compag.2004.03.002>
- Annan, A. P., & Jackson, S. R. (2017). The WARR machine. In A. Giannopoulos & C. Warren (Eds.), *2017 9th International Workshop on Advanced Ground Penetrating Radar (IWAGPR)*. Piscataway, NJ: Institute of Electrical and Electronic Engineers. <https://doi.org/10.1109/IWAGPR.2017.7996106>
- Babcock, E. L., Annan, A. P., & Bradford, J. H. (2016). Cable effects in ground-penetrating radar data and implications for quantitative amplitude measurements. *Journal of Environmental and Engineering Geophysics*, 21, 99–104. <https://doi.org/10.2113/JEEG21.3.99>
- Berard, B. A., & Maillol, J.-M. (2007). Multi-offset ground penetrating radar data for improved imaging in areas of lateral complexity: Application at a Native American site. *Journal of Applied Geophysics*, 62, 167–177. <https://doi.org/10.1016/j.jappgeo.2006.10.002>
- Bogena, H. R. (2016). TERENO: German network of terrestrial environmental observatories. *Journal of Large-Scale Research Facilities*, 2. <http://doi.org/10.17815/jlsrf-2-98>
- Bradford, J. H. (2006). Applying reflection tomography in the postmigration domain to multifold ground-penetrating radar data. *Geophysics*, 71, K1–K8. <https://doi.org/10.1190/1.2159051>
- Bradford, J. H. (2008). Measuring water content heterogeneity using multifold GPR with reflection tomography. *Vadose Zone Journal*, 7, 184–193. <https://doi.org/10.2136/vzj2006.0160>
- Bradford, J. H., Clement, W. P., & Barrash, W. (2009). Estimating porosity with ground-penetrating radar reflection tomography: A controlled 3-D experiment at the Boise Hydrogeophysical Research Site. *Water Resources Research*, 45(4). <https://doi.org/10.1029/2008WR006960>
- Bradford, J. H., Nichols, J., Mikesell, T. D., & Harper, J. T. (2017). Continuous profiles of electromagnetic wave velocity and water content in glaciers: An example from Bench Glacier, Alaska, USA. *Annals of Glaciology*, 50, 1–9. <https://doi.org/10.3189/172756409789097540>
- Brandt, O., Langley, K., Kohler, J., & Hamran, S.-E. (2007). Detection of buried ice and sediment layers in permafrost using multi-frequency ground penetrating radar: A case examination on Svalbard. *Remote Sensing of Environment*, 111, 212–227. <https://doi.org/10.1016/j.rse.2007.03.025>
- Brunet, P., Clement, R., & Bouvier, C. (2010). Monitoring soil water content and deficit using electrical resistivity tomography (ERT): A case study in the Cevennes area, France. *Journal of Hydrology*, 380, 146–153. <https://doi.org/10.1016/j.jhydrol.2009.10.032>
- Busch, S., Van der Kruk, J., & Vereecken, H. (2014). Improved characterization of fine-texture soils using on-ground GPR full-waveform inversion. *IEEE Transactions on Geoscience and Remote Sensing*, 52, 3947–3958. <https://doi.org/10.1109/TGRS.2013.2278297>
- Cherici, C., Kuang, X., Poletti, M., & Rucci, M. (2012). Precision of sustained fixation in trained and untrained observers. *Journal of Vision*, 12, 31–31. <https://doi.org/10.1167/12.6.31>
- Corwin, D. L., & Lesch, S. M. (2005). Apparent soil electrical conductivity measurements in agriculture. *Computers and Electronics in Agriculture*, 46, 11–43. <https://doi.org/10.1016/j.compag.2004.10.005>
- Dabas, M., & Tabbagh, A. (2003). A comparison of EMI and DC methods used in soil mapping: Theoretical considerations for precision agriculture. In J. Stafford & A. Warner (Eds.), *Precision agriculture* (pp. 121–127). Wageningen, the Netherlands: Wageningen Academic Publishers.
- Dal Bo, I., Klotzsche, A., Schaller, M., Ehlers, T. A., Kaufmann, M. S., Fuentes Espoz, J. P., ... van der Kruk, J. (2019). Geophysical imaging of regolith in landscapes along a climate and vegetation gradient in the Chilean coastal cordillera. *CATENA*, 180, 146–159. <https://doi.org/10.1016/j.catena.2019.04.023>
- De Benedetto, D., Castrignano, A., Sollitto, D., Modugno, F., Buttafuoco, G., & Papa, G. I. (2012). Integrating geophysical and geostatistical techniques to map the spatial variation of clay. *Geoderma*, 171–172, 53–63. <https://doi.org/10.1016/j.geoderma.2011.05.005>
- Diamanti, N., Elliott, E. J., Jackson, S. R., & Annan, A. P. (2018). The WARR machine: System design, implementation and data. *Journal of Environmental and Engineering Geophysics*, 23, 469–487.
- Dix, C. H. (1955). Seismic velocities from surface measurements. *Geophysics*, 20, 68–86. <https://doi.org/10.1190/1.1438126>
- Fisher, E., McMechan, G. A., & Annan, A. P. (1992). Acquisition and processing of wide-aperture ground-penetrating radar data. *Geophysics*, 57, 495–504. <https://doi.org/10.1190/1.1443265>
- Forte, E., & Pipan, M. (2016). Review of multi-offset GPR applications: Data acquisition, processing and analysis. *Signal Processing*, 132, 210–220. <https://doi.org/10.1016/j.sigpro.2016.04.011>
- Galagedara, L. W., Redman, J. D., Parkin, G. W., Annan, A. P., & Endres, A. L. (2005). Numerical modeling of GPR to determine the direct ground wave sampling depth. *Vadose Zone Journal*, 4, 1096–1106. <https://doi.org/10.2136/vzj2004.0143>
- Gerhards, H., Wollschläger, U., Yu, Q., Schiwek, P., Pan, X., & Roth, K. (2008). Continuous and simultaneous measurement of reflector depth and average soil-water content with multichannel ground-penetrating radar. *Geophysics*, 73, J15–J23. <https://doi.org/10.1190/1.2943669>
- Gong, Y., Cao, Q., & Sun, Z. (2003). The effects of soil bulk density, clay content and temperature on soil water content measurement using time-domain reflectometry. *Hydrological Processes*, 17, 3601–3614. <https://doi.org/10.1002/hyp.1358>
- Grote, K., Hubbard, S., & Rubin, Y. (2003). Field-scale estimation of volumetric water content using ground-penetrating radar ground wave techniques. *Water Resources Research*, 39(11). <https://doi.org/10.1029/2003WR002045>
- Heincke, B., Green, A. G., Van Der Kruk, J., & Willenberg, H. (2006). Semblance-based topographic migration (SBTM): A method for identifying fracture zones in 3D georadar data. *Near Surface Geophysics*, 4, 79–88. <https://doi.org/10.3997/1873-0604.2005034>



- Huisman, J., Hubbard, S., Redman, J., & Annan, A. (2003). Measuring soil water content with ground penetrating radar. *Vadose Zone Journal*, 2, 476–491. <https://doi.org/10.2136/vzj2003.4760>
- Huisman, J., Sperl, C., Bouten, W., & Verstraten, J. (2001). Soil water content measurements at different scales: Accuracy of time domain reflectometry and ground-penetrating radar. *Journal of Hydrology*, 245, 48–58. [https://doi.org/10.1016/S0022-1694\(01\)00336-5](https://doi.org/10.1016/S0022-1694(01)00336-5)
- Jol, H. M. (2008). *Ground penetrating radar: Theory and applications*. Amsterdam: Elsevier. <https://doi.org/10.1016/B978-0-444-53348-7.X0001-4>
- Klotzsche, A., Jonard, F., Looms, M., van der Kruk, J., & Huisman, J. (2018). Measuring soil water content with ground penetrating radar: A decade of progress. *Vadose Zone Journal*, 17. <https://doi.org/10.2136/vzj2018.03.0052>
- Luo, S., & Hale, D. (2012). Velocity analysis using weighted semblance. *Geophysics*, 77, U15–U22. <https://doi.org/10.1190/geo2011-0034.1>
- Mangel, A., Moysey, S., Ryan, J., & Tarbutton, J. (2012). Multi-offset ground-penetrating radar imaging of a lab-scale infiltration test. *Hydrology & Earth System Sciences*, 16, 4009–4022. <https://doi.org/10.5194/hess-16-4009-2012>
- Muller, W. B. (2018). Semi-automatic determination of layer depth, permittivity and moisture content for unbound granular pavements using multi-offset 3-D GPR. *International Journal of Pavement Engineering*, 19, 1–16. <https://doi.org/10.1080/10298436.2018.1539485>
- Neal, A., & Roberts, C. L. (2000). Applications of ground-penetrating radar (GPR) to sedimentological, geomorphological and geoarchaeological studies in coastal environments. *Geological Society, London, Special Publications*, 175, 139–171. <https://doi.org/10.1144/GSL.SP.2000.175.01.12>
- Oimbe, S., Ingle, R., & Awale, R. (2018). Detection of soil water content using continuous wave ground penetrating radar. *International Journal on Informatics Visualization*, 2, 44–50. <https://doi.org/10.30630/ijov.2.1.104>
- Pan, X., You, Y., Roth, K., Guo, L., Wang, X., & Yu, Q. (2014). Mapping permafrost features that influence the hydrological processes of a thermokarst lake on the Qinghai-Tibet Plateau, China. *Permafrost and Periglacial Processes*, 25, 60–68. <https://doi.org/10.1002/ppp.1797>
- Pettinelli, E., Di Matteo, A., Mattei, E., Crocco, L., Soldovieri, F., Redman, J. D., & Annan, A. P. (2009). GPR response from buried pipes: Measurement on field site and tomographic reconstructions. *IEEE Transactions on Geoscience and Remote Sensing*, 47, 2639–2645. <https://doi.org/10.1109/TGRS.2009.2018301>
- Qin, Y., Chen, X., Zhou, K., Klenk, P., Roth, K., & Sun, L. (2013). Ground-penetrating radar for monitoring the distribution of near-surface soil water content in the Gurbantünggüt Desert. *Environmental Earth Sciences*, 70, 2883–2893. <https://doi.org/10.1007/s12665-013-2528-3>
- Roth, K., Schulm, R., Fluhler, H., & Attinger, W. (1990). Calibration of time domain reflectometry for water-content measurement using a composite dielectric approach. *Water Resources Research*, 26, 2267–2273. <https://doi.org/10.1029/WR026i010p02267>
- Rudolph, S., van der Kruk, J., von Hebel, C., Ali, M., Herbst, M., Montzka, C., ... Weihermüller, L. (2015). Linking satellite derived LAI patterns with subsoil heterogeneity using large-scale ground-based electromagnetic induction measurements. *Geoderma*, 241, 262–271. <https://doi.org/10.1016/j.geoderma.2014.11.015>
- Srinivasan, A. (2006). Precision agriculture: An overview. In A. Srinivasan (Ed.), *Handbook of precision agriculture: Principles and applications* (pp. 3–18). Boca Raton, FL: CRC Press.
- Topp, G. C., Davis, J., & Annan, A. P. (1980). Electromagnetic determination of soil water content: Measurements in coaxial transmission lines. *Water Resources Research*, 16, 574–582. <https://doi.org/10.1029/WR016i003p00574>
- Trinks, I., Hinterleitner, A., Neubauer, W., Nau, E., Löcker, K., Wallner, M., ... Schiel, H. (2018). Large-area high-resolution ground-penetrating radar measurements for archaeological prospection. *Archaeological Prospection*, 25, 171–195. <https://doi.org/10.1002/arp.1599>
- Vachaud, G., Passerat de Silans, A., Balabanis, P., & Vauclin, M. (1985). Temporal stability of spatially measured soil water probability density function. *Soil Science Society of America Journal*, 49, 822–828. <https://doi.org/10.2136/sssaj1985.03615995004900040006x>
- van Overmeeren, R., Sariowan, S., & Gehrels, J. (1997). Ground penetrating radar for determining volumetric soil water content; results of comparative measurements at two test sites. *Journal of Hydrology*, 197, 316–338. [https://doi.org/10.1016/S0022-1694\(96\)03244-1](https://doi.org/10.1016/S0022-1694(96)03244-1)
- Vereecken, H., Huisman, J., Bogaen, H., Vanderborght, J., Vrugt, J., & Hopmans, J. (2008). On the value of soil moisture measurements in vadose zone hydrology: A review. *Water Resources Research*, 44(4). <https://doi.org/10.1029/2008WR006829>
- von Hebel, C., Rudolph, S., Mester, A., Huisman, J. A., Kumbhar, P., Vereecken, H., & van der Kruk, J. (2014). Three-dimensional imaging of subsurface structural patterns using quantitative large-scale multiconfiguration electromagnetic induction data. *Water Resources Research*, 50, 2732–2748. <https://doi.org/10.1002/2013WR014864>
- von Hebel, C., van der Kruk, J., Huisman, J. A., Mester, A., Altdorff, D., Endres, A. L., ... Vereecken, H. (2019). Calibration, conversion, and quantitative multi-layer inversion of multi-coil rigid-boom electromagnetic induction data. *Sensors*, 19, 4753. <https://doi.org/10.3390/s19214753>
- Warren, C., Giannopoulos, A., & Giannakis, I. (2016). gprMax: Open source software to simulate electromagnetic wave propagation for ground penetrating radar. *Computer Physics Communications*, 209, 163–170. <https://doi.org/10.1016/j.cpc.2016.08.020>
- Weihermüller, L., Huisman, J., Lambot, S., Herbst, M., & Vereecken, H. (2007). Mapping the spatial variation of soil water content at the field scale with different ground penetrating radar techniques. *Journal of Hydrology*, 340, 205–216. <https://doi.org/10.1016/j.jhydrol.2007.04.013>
- Wollschläger, U., Gerhards, H., Yu, Q., & Roth, K. (2010). Multi-channel ground-penetrating radar to explore spatial variations in thaw depth and moisture content in the active layer of a permafrost site. *The Cryosphere*, 4, 269–283. <https://doi.org/10.5194/tc-4-269-2010>
- Yelf, R. (2004). Where is true time zero? In E. Slob, A. Yarovoy, & J. Rhebergen (Eds.), *Proceedings of the Tenth International Conference on Ground Penetrating Radar* (Vol. 1, pp. 279–282). IEEE.
- Yilmaz, Ö (2001). *Seismic data analysis: Processing, inversion, and interpretation of seismic data*. Tulsa, OK: Society of Exploration Geophysicists. <https://doi.org/10.1190/1.9781560801580>

- Zacharias, S., Bogen, H., Samaniego, L., Mauder, M., Fuß, R., Pütz, T., ... Butterbach-Bahl, K. (2011). A network of terrestrial environmental observatories in Germany. *Vadose Zone Journal*, 10, 955–973. <https://doi.org/10.2136/vzj2010.0139>
- Zhu, X., Shao, M. a., & Liang, Y. (2018). Spatiotemporal characteristics and temporal stability of soil water in an alpine meadow on the northern Tibetan Plateau. *Canadian Journal of Soil Science*, 98, 161–174. <https://doi.org/10.1139/CJSS-2017-0078>

**How to cite this article:** Kaufmann MS, Klotzsche A, Vereecken H, van der Kruk J. Simultaneous multichannel multi-offset ground-penetrating radar measurements for soil characterization. *Vadose Zone J.* 2020;19:e20017. <https://doi.org/10.1002/uar2.20017>